REPORT DOCUMENTATION PAGE

Form Approved OMB NO. 0704-0188

1. REPORT DATE (DD-MM-YYYY)	2. REPORT TYPE	3. DATES COVERED (From - To)
	Technical Report	-

4. TITLE AND SUBTITLE
Multi-linear Stress Strain and Closed-form Moment Curvature Response of Epoxy Resins

5a. CONTRACT NUMBER
W911NF-07-1-0132

5b. GRANT NUMBER

5c. PROGRAM ELEMENT NUMBER
611102

6. AUTHORS
Masoud Yekani Fard, Yingtao Liu, Aditi Chattopadhyay

5d. PROJECT NUMBER

5e. TASK NUMBER

5f. WORK UNIT NUMBER

7. PERFORMING ORGANIZATION NAMES AND ADDRESSES
Arizona State University
Office of Research & Sponsored Projects Administration
Arizona State University
Tempe, AZ 85287 -3503

8. PERFORMING ORGANIZATION REPORT NUMBER

9. SPONSORING/MONITORING AGENCY NAME(S) AND ADDRESS(ES)
U.S. Army Research Office
P.O. Box 12211
Research Triangle Park, NC 27709-2211

10. SPONSOR/MONITOR'S ACRONYM(S)
ARO

11. SPONSOR/MONITOR'S REPORT NUMBER(S)
49008-EG.3

12. DISTRIBUTION AVAILIBILITY STATEMENT
Approved for Public Release; Distribution Unlimited

13. SUPPLEMENTARY NOTES
The views, opinions and/or findings contained in this report are those of the author(s) and should not contrued as an official Department of the Army position, policy or decision, unless so designated by other documentation.

14. ABSTRACT
A simplified multi-linear stress strain approach has been used to obtain the closed form nonlinear moment curvature response for epoxy resin materials. The model consists of constant plastic flow in tension and constant yield in compression. The multi-linear stress strain model is described by two main parameters in addition to four non-dimensional tensile and five non-dimensional compressive parameters. The main parameters are modulus of elasticity in tension and strain at the proportional elastic limit point in tension. The nine non-dimensional

15. SUBJECT TERMS
epoxy resins, stress strain relation, moment curvature, material properties, plastic flow, nonlinear behavior, flexural response, load deflection, three point bending

16. SECURITY CLASSIFICATION OF:			17. LIMITATION OF ABSTRACT	15. NUMBER OF PAGES	19a. NAME OF RESPONSIBLE PERSON
a. REPORT	b. ABSTRACT	c. THIS PAGE			Aditi Chattopadhyay
UU	UU	UU	UU		19b. TELEPHONE NUMBER 480-965-9342

Standard Form 298 (Rev 8/98)
Prescribed by ANSI Std. Z39.18

Report Title

Multi-linear Stress Strain and Closed-form Moment Curvature Response of Epoxy Resins

ABSTRACT

A simplified multi-linear stress strain approach has been used to obtain the closed form nonlinear moment curvature response for epoxy resin materials. The model consists of constant plastic flow in tension and constant yield in compression. The multi-linear stress strain model is described by two main parameters in addition to four non-dimensional tensile and five non-dimensional compressive parameters. The main parameters are modulus of elasticity in tension and strain at the proportional elastic limit point in tension. The nine non-dimensional parameters are strain at the ultimate tensile stress, maximum strain, post elastic proportionality stiffness, and post peak strength in the tension model and strain at the proportionality elastic limit, strain at yield strength point, maximum strain, initial elastic stiffness and post elastic proportionality stiffness in the compression model. Explicit expressions are derived for the stress-strain behavior of the polymers. Closed form equations for moment curvature relationship are presented. The results of tension, compression, and bending tests using digital image correlation technique are presented. Load deflection response of flexural three point bending (3PB) samples could be predicted using the moment curvature equations, crack localization rules, and fundamental static equations. The proposed nonlinear moment curvature shows good predictions when compared to experimental results.

Multi-linear Stress Strain and Closed-form Moment Curvature Response of Epoxy Resins

Masoud Yekani Fard[1a], Yingtao Liu[a], and Aditi Chattopadhyay[a]
[a]School of Mechanical, Aerospace, Chemical and Materials Eng., Arizona State University, AZ, USA

Abstract

A simplified multi-linear stress strain approach has been used to obtain the closed form nonlinear moment curvature response for epoxy resin materials. The model consists of constant plastic flow in tension and constant yield in compression. The multi-linear stress strain model is described by two main parameters in addition to four non-dimensional tensile and five non-dimensional compressive parameters. The main parameters are modulus of elasticity in tension and strain at the proportional elastic limit point in tension. The nine non-dimensional parameters are strain at the ultimate tensile stress, maximum strain, post elastic proportionality stiffness, and post peak strength in the tension model and strain at the proportionality elastic limit, strain at yield strength point, maximum strain, initial elastic stiffness and post elastic proportionality stiffness in the compression model. Explicit expressions are derived for the stress-strain behavior of the polymers. Closed form equations for moment curvature relationship are presented. The results of tension, compression, and bending tests using digital image correlation technique are presented. Load deflection response of flexural three point bending (3PB) samples could be predicted using the moment curvature equations, crack localization rules, and fundamental static equations. The proposed nonlinear moment curvature shows good predictions when compared to experimental results.

Keywords epoxy resins, stress strain relation, moment curvature, material properties, plastic flow, nonlinear behavior, flexural response, load deflection, three point bending

Introduction

Epoxy resins are one of the frequent matrix materials in fiber composites. Mechanical properties (stress strain relationship) and progressive failure is still a challenge for researchers. Difficulty of a constitutive law in polymer matrix composites is mainly due to the characterization of polymer mechanical behavior. The hydrostatic component of stress has a significant effect on the load deformation response of resins even at low levels of stress. Hydrostatic stresses are known to affect the yield stress and nonlinear response of polymers; the absolute value of the yield stress in compression is higher than the ultimate tensile stress. In order to develop a general model for polymer composite materials, the behavior of polymer resins under different types of loading has to be understood. Wineman and Rajagopal[9] (2000) used a viscoplasticity model to capture the polymer behavior. Zhang and Moore[10] (1997) used the Bodner–Partom internal state variable model originally developed for metals to obtain the nonlinear uniaxial tensile response of polyethylene. By modifying the definitions of the effective stress and

[1] Masoud.yekanifard@asu.edu

effective inelastic strain rate in the Drucker-Prager yield criteria, Li and Pan[5] (1990), Chang and Pan[1] (1997), and Hsu et al.[3](1999) developed a viscoplasticity approach for the constitutive law of polymer materials. Gilat et al.[2] (2007) used an internal state variable model to modify the Bodner model to capture the effects of hydrostatic stresses on the response. In their approach, a single unified strain variable is defined to represent all inelastic strains. Jordan et al.[4] (2008) modified the original Mulliken-Boyce[7] model (2006) for one dimension to capture the compressive mechanical properties of polymer composites. The original model is a three dimensional strain rate and temperature dependent model for thermoplastic polymers. The majority of the parameters were determined by fitting the model to experimental compressive data. In this study, the flexural behavior of a beam is investigated in an attempt to establish a relationship between the tensile and compressive stress strain curves in one side and moment curvature response of epoxy resin material in the other side. In order to correlate tension, compression stress strain curves and flexural data, a closed form solution has been developed to obtain moment curvature response. The load deflection response for nonlinear materials under determinate static conditions has been developed. Using inverse analysis, the effect of stress gradient on the multi-linear stress strain curve obtained from the in-plane uniaxial tests has been studied.

Tension and Compression Multi-linear Stress Strain Curve

The multi-linear stress strain curve for tension and compression is bilinear up to the peak stress. Figure 1 shows the simplified tension and compression stress-strain relationship of epoxy resin materials. The tension and compression curves are defined uniquely by the parameters E, ε_{PEL}, μ_{t1}, μ_{Ut}, α, ω, γ, β, μ_{co}, μ_{c1}, and μ_{Uc}. The tensile stress at the proportionality elastic point (PEL) is related empirically to the stress at the ultimate tensile strength (UTS) point. The ascending part of the tension and compression stress strain diagrams consist of two linear parts: 0 to PEL, and PEL to UTS in tension or PEL to compressive yield stress (CYS) in compression. The curve after peak strength is idealized as horizontal with σ_f and σ_{CYS} as the post peak sustained stress in tension and constant yield strength in compression respectively. The constant post peak tensile stress level ω shows the ability of the model to represent a continuous (ω=1) or discontinuous stress response. The post peak response in tension terminates at the ultimate tension strain level ($\varepsilon_{Ut} = \mu_{Ut}\ \varepsilon_{PEL}$), and for compression it ends at ultimate compression strain level ($\varepsilon_{Uc} = \mu_{Uc}\ \varepsilon_{PEL}$). In the elastic range, the resin beam in bending could be treated as a bi-modulus material with different moduli in tension and compression. The tension and compression stress strain relationship are defined as shown in table 1.

Table 1. Multi-linear stress strain curve

Stress	Definition	Domain of strain
$\sigma_t(\varepsilon_t)$	$E\varepsilon_t$	$0 \le \varepsilon_t \le \varepsilon_{PEL}$
	$E\ (\varepsilon_{PEL} + \alpha\ (\varepsilon_t - \varepsilon_{PEL}))$	$\varepsilon_{PEL} < \varepsilon_t \le \mu_{t1}\ \varepsilon_{PEL}$
	$\omega E\ \varepsilon_{PEL}$	$\mu_{t1}\ \varepsilon_{PEL} < \varepsilon_t \le \mu_{Ut}\ \varepsilon_{PEL}$
	0	$\mu_{Ut}\ \varepsilon_{PEL} < \varepsilon_t$
$\sigma_c(\varepsilon_c)$	$\gamma E\ \varepsilon_c$	$0 \le \varepsilon_c \le \mu_{c0}\ \varepsilon_{PEL}$

	$E\ (\gamma\ \mu_{c0}\ \varepsilon_{PEL} + \beta\ (\ \varepsilon_c - \mu_{c0}\ \varepsilon_{PEL}))$	$\mu_{c0}\ \varepsilon_{PEL} < \varepsilon_c \leq \mu_{c1}\ \varepsilon_{PEL}$
	$E\ \varepsilon_{PEL}\ (\ \beta\ \mu_{c1} + \mu_{c0}\ (\gamma - \beta))$	$\mu_{c1}\ \varepsilon_{PEL} < \varepsilon_c \leq \mu_{Uc}\ \varepsilon_{PEL}$
	0	$\mu_{Uc}\ \varepsilon_{PEL} < \varepsilon_c$

σ_c, σ_t, ε_c, and ε_t are compression and tension stresses and strains respectively. The nine normalized parameters used in the definition of the constitutive law are defined by

$$\mu_{c0} = \frac{\varepsilon_{PEL,c}}{\varepsilon_{PEL}},\ \mu_{c1} = \frac{\varepsilon_{CYS}}{\varepsilon_{PEL}},\ \mu_{Uc} = \frac{\varepsilon_{Uc}}{\varepsilon_{PEL}},\ \mu_{t1} = \frac{\varepsilon_{Uts}}{\varepsilon_{PEL}}, \mu_{Ut} = \frac{\varepsilon_{Ut}}{\varepsilon_{PEL}} \tag{1}$$

$$\gamma = \frac{E_c}{E},\ \ \beta = \frac{E_{PEL,c}}{E},\ \ \alpha = \frac{E_{PEL,t}}{E} \tag{2}$$

$$\omega = \frac{\sigma_f}{\sigma_{PEL}} \tag{3}$$

Using classical beam theory, linear distribution of strain across the depth is assumed. The stress and strain distribution across a section of a beam with depth *h* and width *b* by imposing normalized top compressive strain in different cases are shown in Figure 2. Normalized heights of compression and tension sub-zones with respect to beam depth *h* are shown in Table 2. Tables 3 and 4 present the normalized stress at the vertices of the tension and compression sub-zones with respect to tensile stress at the proportionality limit point. The internal force in each compression and tension sub-zone of nine stress distribution cases is calculated from the stress diagram and the normalized form with respect to the tension force at the proportionality limit point ($bhE\varepsilon_{PEL}$) is presented in Tables 5 and 6. The centroid of the stress in each sub-zone represents the line of action and moment arm respect to the neutral axis and is presented in the normalized form in Tables 7 and 8.

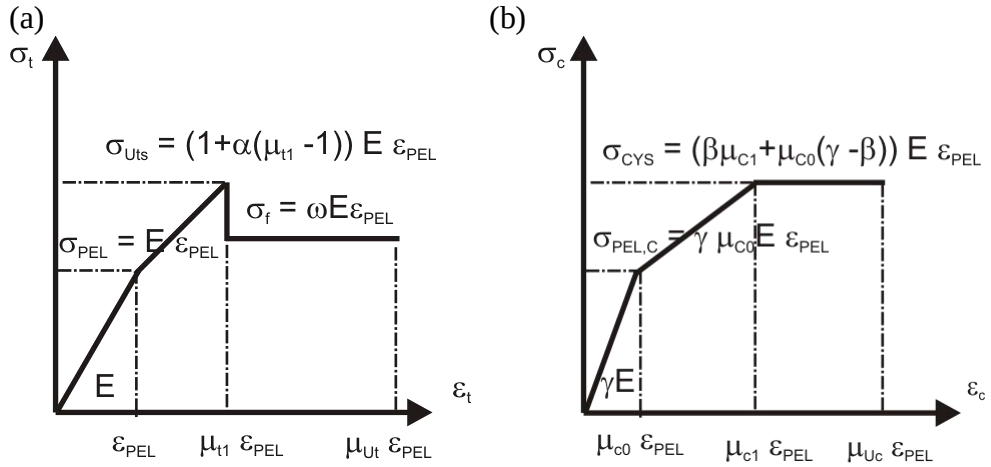

Figure 1. (a) constant flow in tension; (b) constant yield in compression

(a) rectangular cross section

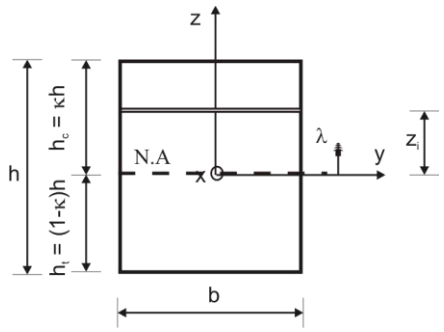

(b) case one

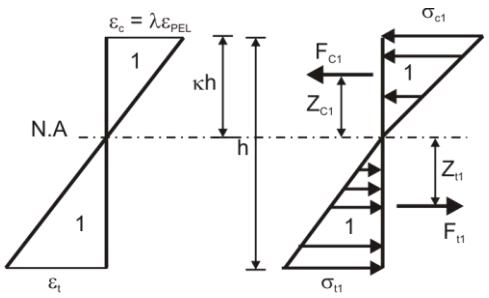

(c) case two

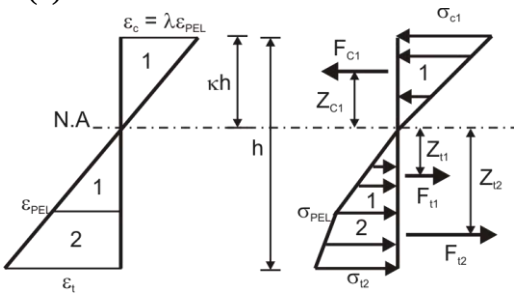

(d) case three

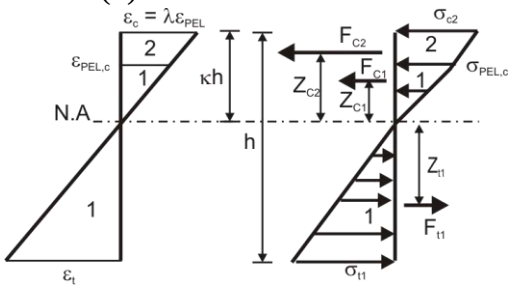

(e) case four

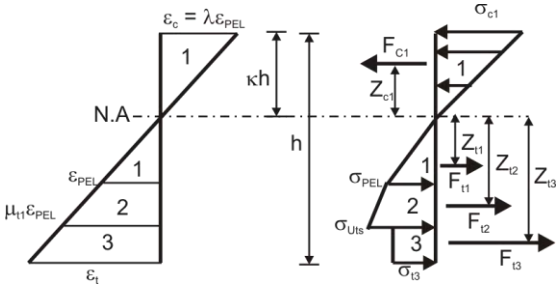

(f) case five

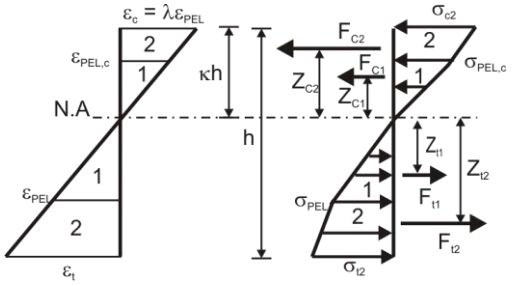

(g) case six

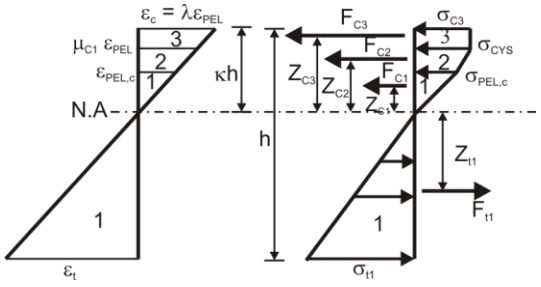

(h) case seven

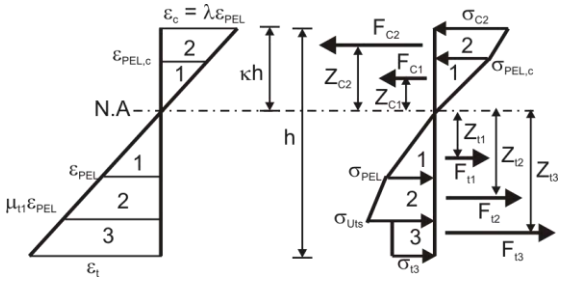

(i) case eight (j) case nine

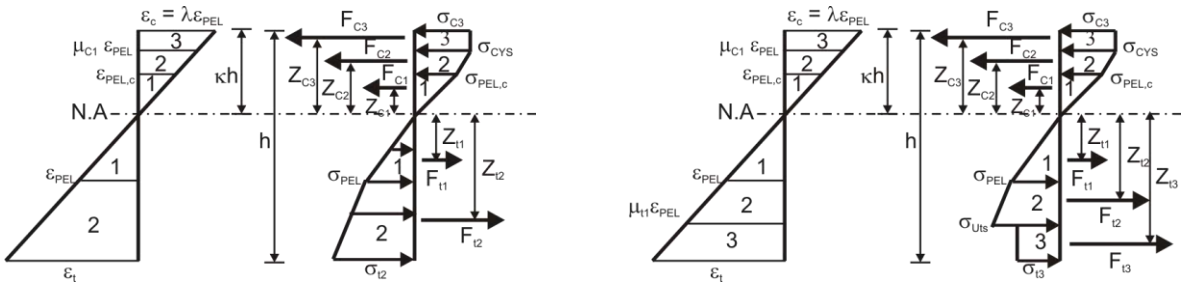

Figure 2. (a) rectangular cross section, (b) to (j) stress strain distributions across the cross section for different cases.

Closed-form Moment Curvature Response

The development of stress strain across the section by increasing the normalized compressive strain is presented in Figure 3. Stress strain develops at least to stage 4 where compressive and tensile failure is possible if $\lambda_{max} = \mu_{Uc}$ in case 6, or $\lambda_{max} = F$ in case 4. Moving through different stages in Figure 3 depends on the controlling value for λ_{max}. Using the auxiliary points defined in Table 9, the transition points defined as tp_{ij} between different stages in Figure 3 could be presented by the following equations.

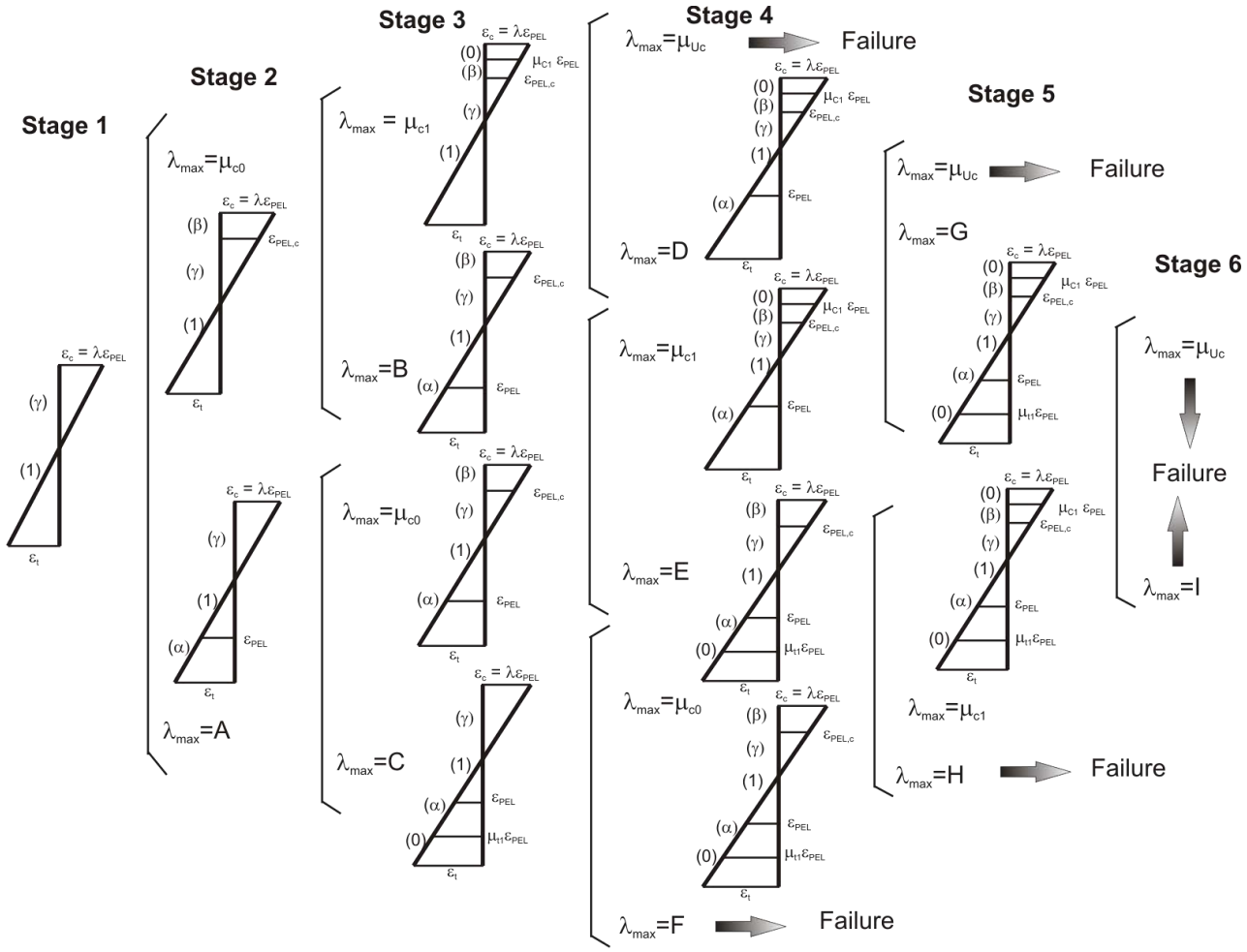

Figure 3. Strain development in the cross section at the different stages of loading

$$
\begin{aligned}
tp_{12} &= Min(\mu_{c0}, A) \\
tp_{23} &= Min(\mu_{c0}, C) \ or \ Min(\mu_{c1}, B) \\
tp_{34} &= Min(\mu_{Uc}, D) \ or \ Min(\mu_{c1}, E) \ or \ Min(\mu_{c0}, F) \\
tp_{45} &= Min(\mu_{Uc}, G) \ or \ Min(\mu_{c1}, H) \\
tp_{56} &= Min(\mu_{Uc}, I)
\end{aligned}
\tag{4}
$$

Where indexes i and j refer to origin and destination stages respectively. The net force is obtained as the difference between the tension and compression forces in Table 3, equated to zero for internal equilibrium, and solved for the neutral axis depth ratio defined as κ. The expressions of net force in some stages result in more than one solutions for κ. Using a large scale of numerical tests covering possible ranges of material parameters, the solution of κ which yields the valid value $0 < \kappa < 1$ was determined and presented in Table 10. Moment expressions are obtained by taking the first moment of the compression and tension forces about the neutral axis. Curvature is calculated by dividing the top compressive strain by the depth of the neutral axis κh. The closed form solutions for normalized moment M_i and curvature φ_i with respect to the values at the tensile PEL points are presented in Equations 5, 6 and 7 and Table 10.

$$M(\lambda, \gamma, \beta, \alpha, \mu_{c0}, \mu_{c1}, \mu_{t1}, \mu_{Ut}, \mu_{Uc}, \omega) = M_{PEL} M'(\lambda, \gamma, \beta, \alpha, \mu_{c0}, \mu_{c1}, \mu_{t1}, \mu_{Ut}, \mu_{Uc}, \omega) \tag{5}$$

$$\varphi(\lambda, \gamma, \beta, \alpha, \mu_{c0}, \mu_{c1}, \mu_{t1}, \mu_{Ut}, \mu_{Uc}, \omega) = \varphi_{PEL} \varphi'(\lambda, \gamma, \beta, \alpha, \mu_{c0}, \mu_{c1}, \mu_{t1}, \mu_{Ut}, \mu_{Uc}, \omega) \tag{6}$$

$$\varphi'_i(\lambda, \gamma, \beta, \alpha, \mu_{c0}, \mu_{c1}, \mu_{t1}, \mu_{Ut}, \mu_{Uc}, \omega) = \frac{\lambda}{2\kappa_i}, \quad i = 1,2,3,\ldots,9 \tag{7}$$

Where M_{PEL} and φ_{PEL} are moment and curvature (for a material with the same modulus of elasticity in tension and compression) at the tensile PEL and are defined as

$$M_{PEL} = \frac{bh^2 E \varepsilon_{PEL}}{6} \quad , \quad \varphi_{PEL} = \frac{2\varepsilon_{PEL}}{h} \tag{8}$$

The ultimate moment M_u (flexural strength) is computed based on Equations 5, 8 and Table 10. For a ductile material like resin, M_u could approach M_∞ at very large λ values. The normalized moment at the very large λ values M'_∞ is computed by substituting $\lambda = \infty$ in the expression for κ in case nine of Table 10 and by substitution of $\lambda = \infty$ and κ_∞ in the normalized moment expression. Equations 9, 10, and 11 present the values of the neutral axis depth, normalized moment, and curvature for very large λ values.

$$\kappa_\infty = \frac{\omega}{\omega + \gamma\mu_{c0} - \beta\mu_{c0} + \beta\mu_{c1}} \tag{9}$$

$$M'_{\infty} = \frac{3\omega(\gamma\mu_{c0} - \beta\mu_{c0} + \beta\mu_{c1})}{\omega + \gamma\mu_{c0} - \beta\mu_{c0} + \beta\mu_{c1}} \quad (10)$$

$$\varphi'_{\infty} = \infty \quad (11)$$

The neutral axis depth and normalized moment are a function of characteristic points of tension and compression stress strain model (ω, γ,β,μ_{c0}, μ_{c1}). The κ_9 and M'_9 expressions are functions of all characteristic points in the stress strain model but when compressive strain values are large, they are independent of tensile post PEL stiffness (α) and strain of ultimate tensile strength (μ_{t1}). For an elastic perfectly plastic materials with equal tensile and compression elastic moduli and equal yield and post peak flow stress, Equation 9 and 10 yields to 0.5 and 1.5 respectively, validating the theoretical value that the plastic moment capacity of a rectangular section is 1.5 times its elastic yield strength at $\mu_{c0} = \mu_{c1} = \mu_{t1} = 1$ presented by Salmon[8] (1990). For a set of parameters γ,β,μ_{c0}, μ_{c1}, the critical value of ω which results in a flexural capacity in the infinity (before failure) greater than the flexural capacity at the tensile PEL point can be found. By equating the normalized moment for large top compressive strain to one ($M'_{\infty}=1$) the critical value of post peak tension flow, $\omega_{critical}$, is expressed as

$$\omega_{critical} = \frac{\gamma\mu_{c0} - \beta\mu_{c0} + \beta\mu_{c1}}{3(\gamma\mu_{c0} - \beta\mu_{c0} + \beta\mu_{c1}) - 1} \quad (12)$$

Parametric Study

Parametric studies determine the sensitivity of the different parts of the model to the relative behavior of the variables. Although polymer materials show strain softening behavior with a percentage of the ultimate tensile strength[9], a complete set of parametric studies was conducted to examine the strain softening materials. Effect of the tension and compression stress strain relation on the response of polymer materials was addressed by studying the effect of variation of a parameter in the constitutive law while all other parameters were held constant to the typical values. Epon E 862 epoxy resin was chosen and typical mechanical characteristic of E 862 were extracted from Littell et al.[6] (2008) and are shown in Table 11.

Table 11: Typical characteristic values of stress strain curve for E 862

E (MPa)	ε_{PEL} (%)	ε_{Uts} (%)	σ_{Uts} (MPa)	ε_{ut} (%)	σ_f (MPa)	Ec (MPa)	$\varepsilon_{PEL,c}$ (%)	ε_{CYS} (%)	σ_{CYS} (MPa)	ε_{uc} (%)
2069	2.05	7.6	70	24	60.5	2457	1.9	9.2	93	35

The flexural strength and ductility for each material parameter was expressed as the normalized moment curvature response, independent of geometry and tensile PEL strength. Figure 4 shows the results of the parametric study for strain softening material. Figure 4 (a1) to (a3) presents the effect of constant flow tensile strength on the moment curvature and on the location of neutral axis depth. ω = 0.017 and 1.63 correspond to

constant tensile plastic flow equal to 1% and 100% of the ultimate tensile strength respectively. Figure 4 (a2) depicts that moment curvature response is extremely sensitive to the variations in constant tensile flow as the location of maximum flexure and the post peak regime completely changes with ω. The flexural response changes from brittle to ductile behavior as ω increases from 0.017 to 1.63. For the parameters given, Equation 12 yields to $\omega_{critical}$ = 0.39. Figure 4 (a2) also shows that in order to obtain the bending moment at large top compressive strains equal to or greater than the bending capacity at the tensile PEL, the required tensile plastic flow should be equal or greater than ω=0.39 (25% of the ultimate tensile strength). When ω=1.42 the response characterizes exactly the material behavior of Epon E 862, and Equation (10) gives $M'_{\infty} = 2.58$ as it can be seen from Figure 4(a2). Figure 4 (a3) shows that decreasing the level of tensile flow decreases the neutral axis depth, especially for ω values less than 0.5 (30% of UTS). Tensile failure was the governing mechanism in all the material responses. Materials with ω = 0.08 and ω = 0.017 didn't experience compression yield and their stress strain relationship always were in the elastic compression region. This is the reason that their neutral axis depth and moment capacity drops sharply by applying top compressive strain, and they show a brittle material behavior. Table 9, Equation 4 and Figure 3 show that the stress development in the cross section is totally independent of tensile plastic flow in stages 1, 2, 3. Stage 4 would also be independent of ω if $tp_{23} \neq C$ in stage 3. By calculating the transition points, one can find out that $tp_{12} = A$ = 0.9167 in case 2, $tp_{23} = \mu_{c0}$ = 0.93 in case 5, $tp_{34} = E$ = 3.358 in case 7, for all ω values. For ω = 0.017 and 0.08, $tp_{45} = H$ (H(ω=0.017) = 3.43, and H(ω=0.08) = 3.70) and tensile failure happens in stage 5. However, for ω = 0.393, 0.5, 0.83, 1.16, 1.42, 1.49, and 1.62, tp_{45} would be equal to μ_{c1} = 4.49 in case 9 and by comparing I(ω) with μ_{Uc}, all will fail in tension in stage 6. For ω = 0.017 and 0.08 and in stage 5, since H (ω) is less than μ_{c1}, tensile failure happens and top compressive strain is less than μ_{c1}. Figure 4 (b1) to (b3) depicts the effect of UTS on the moment curvature and neutral axis location at constant tensile post PEL slope and constant tensile flow stress. Figure 4(b2) reveals that an increase in μ_{t1}, increases flexural strength and this is clear for high μ_{t1} values. However, the amount of M'_{∞} is not affected as much as the flexural strength since for μ_{t1} > 6 the moment at infinity is less than the flexural strength. Figure 4 (b3) shows that by increasing the ultimate tensile strength, neutral axis moves downward and approaches toward κ = 0.5. One can look at the variation of μ_{t1} as the variation of CYS to UTS ratio which is defined as $\frac{\gamma\mu_{c0} + \beta(\mu_{c1} - \mu_{c0})}{1 + \alpha(\mu_{t1} - 1)}$ and by substituting γ = 1.19, β = 0.3, α =0.24, μ_{c0} = 0.93, μ_{c1} = 4.49, it is clear that changes in μ_{t1} from 2.75 to 8 will change the CYS to UTS ratio from 1.53 to 0.81. Figure 4 (c1) shows the compression and tension model with the post tensile PEL slope and strain of UTS points varied from 0.15 to 0.6, and 5.33 to 2.083 respectively, at fixed UTS and post peak tensile flow. Stress strain models of three sets of α and μ_{t1} are shown in Figure 4 (c1). Figure 4 (c2) reveals that changes in parameters α and μ_{t1} slightly affect the moment but extremely affect position of the neutral axis for a wide range of normalized top compressive strains between 1 and 4 and that will change the stress distribution across the section between elastic and post peak range. In order to study the effect of post compressive PEL stiffness, the range of parameters β and μ_{c1} were used to

represent the variation in β while CYS was constant. The compressive and tensile stress strain models are shown in Figure 4 (d1). Unlike the post tensile PEL stiffness, analyses of Figure 4 (d2) depicts that flexural strength is quite sensitive to the variations in parameter β as it significantly affects the flexural strength. Increasing β and decreasing μ_{c1} slightly affect the ductility as it is shown in Figure 4 (d2). Figure 4 (d3) shows the profile of the neutral axis position versus the applied top compressive strain. Curves of (β = 0.1, μ_{c1} = 11.61) and (β = 0.2, μ_{c1} = 6.27) have completely different shape comparing to others. After λ exceeds the compressive PEL, the neutral axis depth increases sharply to statically equilibrate the axial forces in the cross section but since CYS is greater than UTS and tensile plastic flow, it starts to decrease in post peak regions. Material with (β = 0.1, μ_{c1} = 11.61) did not experience any yield in compression and all are failed in tension. Figure 4 (e1) shows the compressive and tensile stress strain relationship with different β and constant μ_{c1}. CYS is from 62.04 MPa for β = 0.1 to 137.54 MPa for β = 0.6. UTS is 70.2 MPa and constant for all cases. Increasing the compressive yield strength 100%, the flexural capacity increases around 40% as it is shown by the normalized moment curvature plots in Figure 4 (e2). Figure 4 (e3) depicts that for β = 0.1 and 0.2 as CYS is in the range of UTS, the neutral axis is almost in the middle of the section along all loading stages. Analyses indicate that tension is the governing failure mechanism in all cases while compression strain exceeds the yield point. In order to study the effect of initial compressive stiffness, a range of parameters, γ and $\mu_{c0,}$ were coupled to represent the increase in relative compressive to tensile stiffness from 0.8 to 1.4 at a fixed compressive PEL to tensile PEL ratio of $\gamma\mu_{c0}$ = 1.107 as shown in Figure 4 (f1). Figure 4 (f2) and (f3) reveal that changes in the relative stiffness slightly affect the moment curvature and the location of the neutral axis especially in the nonlinear phase. Analyses show that all the cases experience yielding in compression and failure in tension.

(a1)

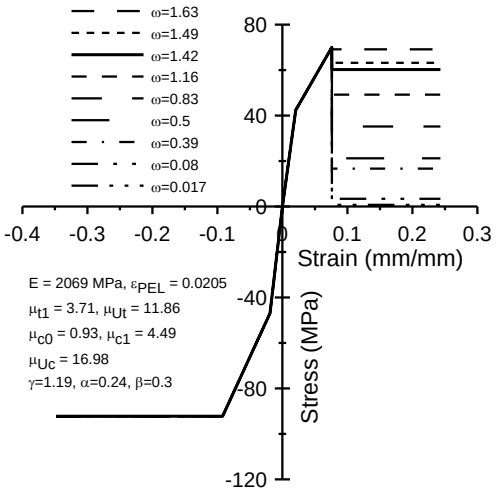

(a2)

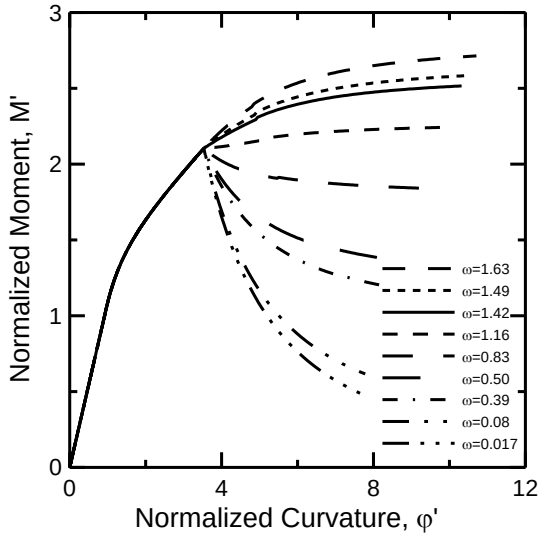

(a3)

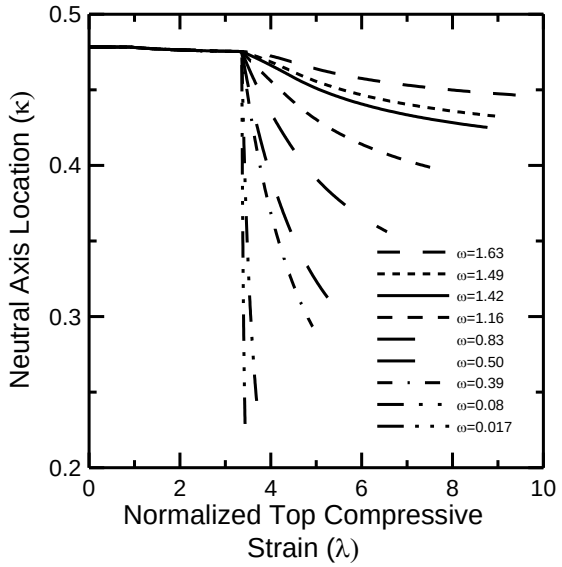

(b1)

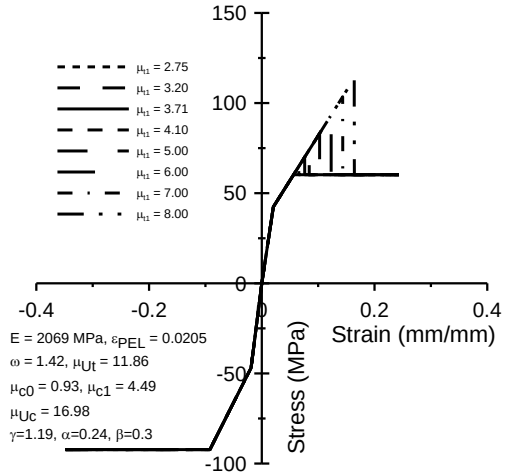

(b2)

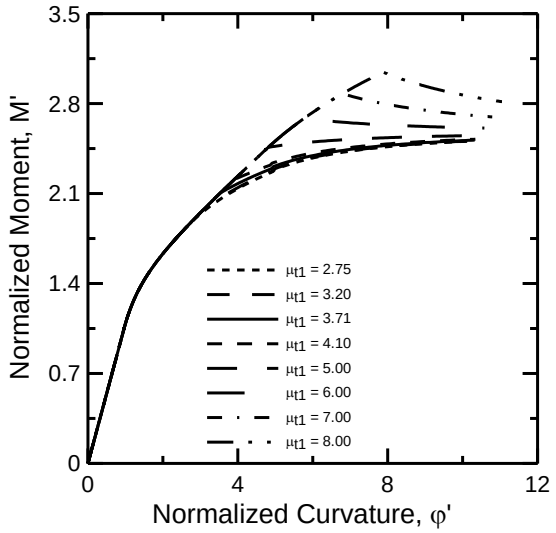

(b3)

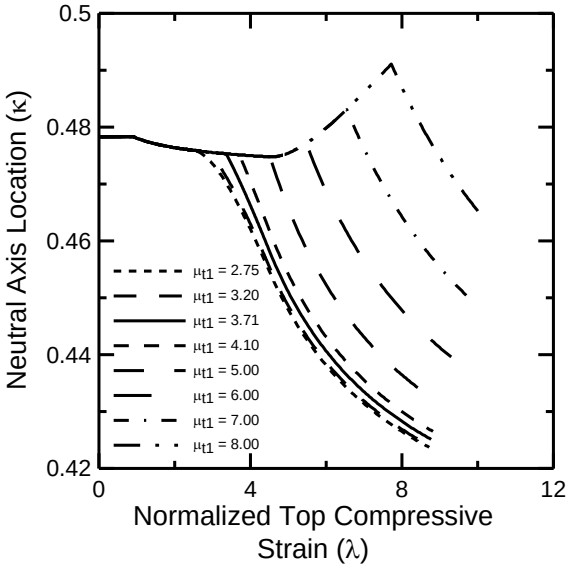

(c1)

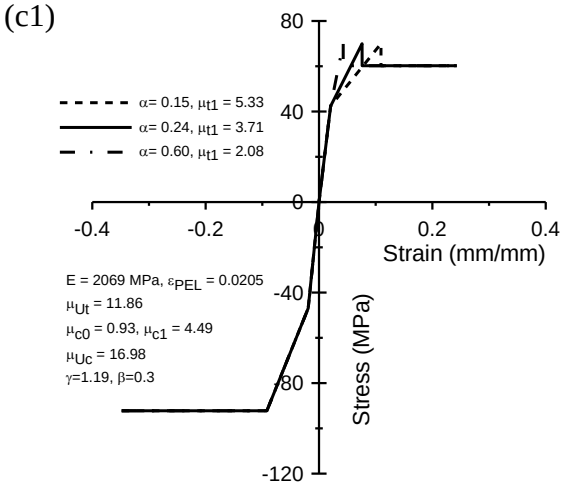

(c2)

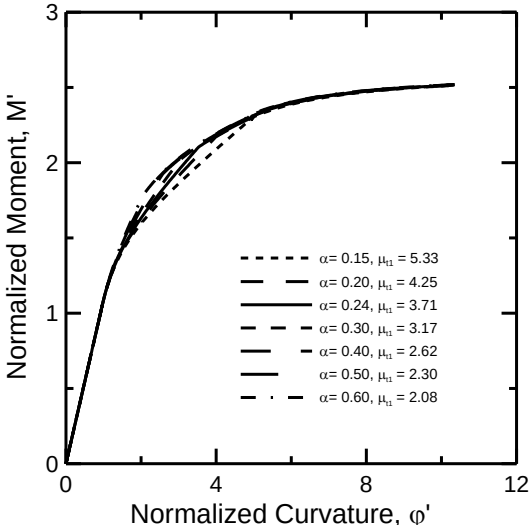

(c3)

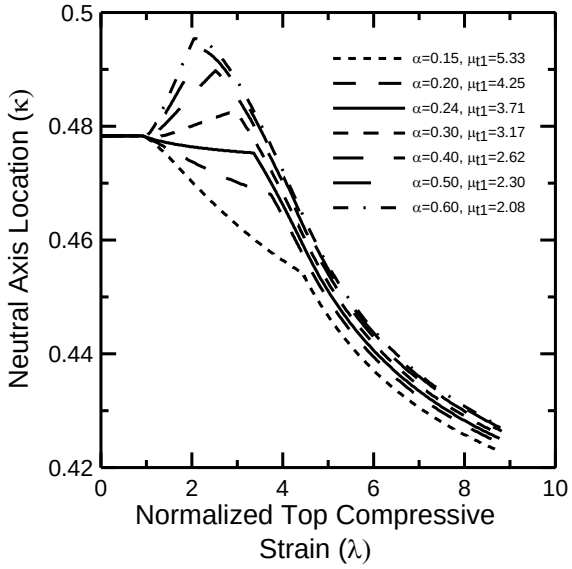

(d1)

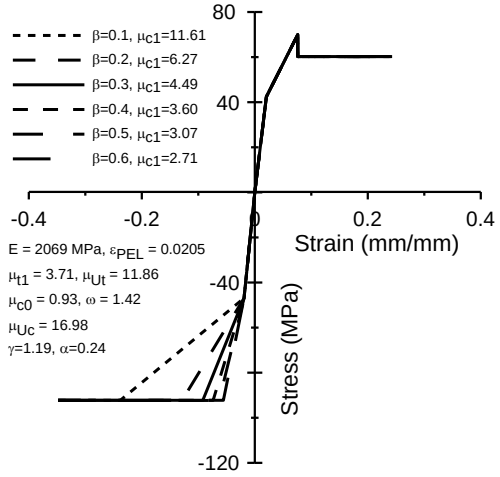

(d2)

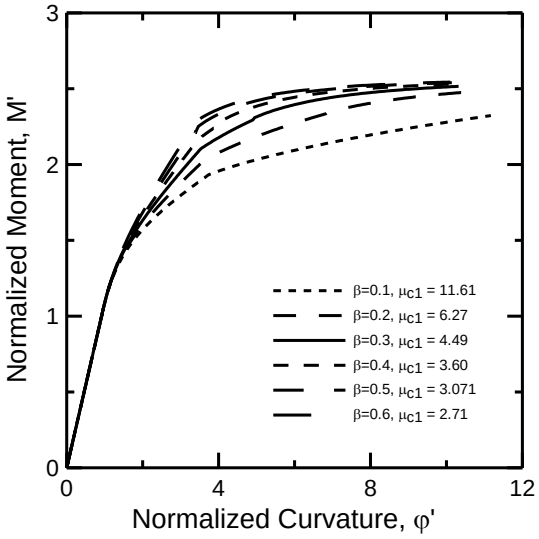

(d3)

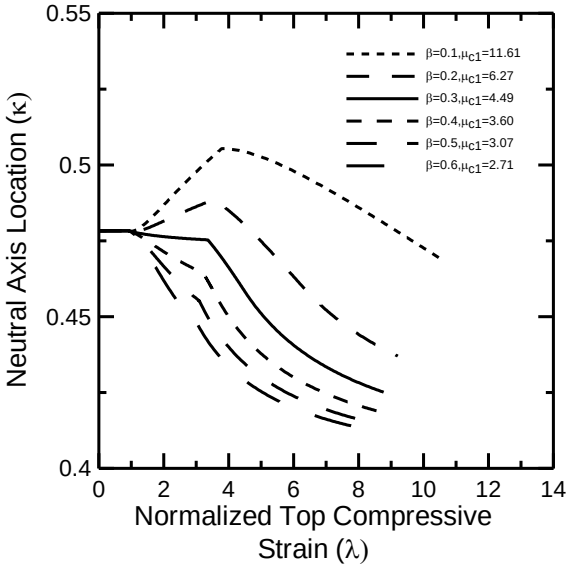

(e1)

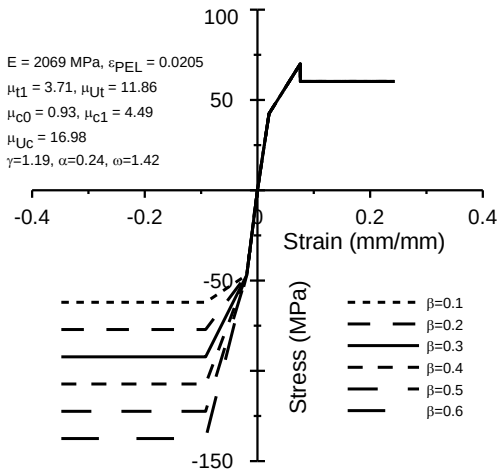

(e2)

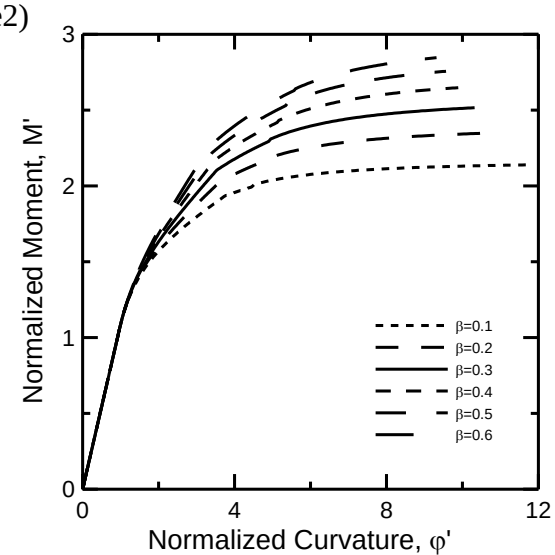

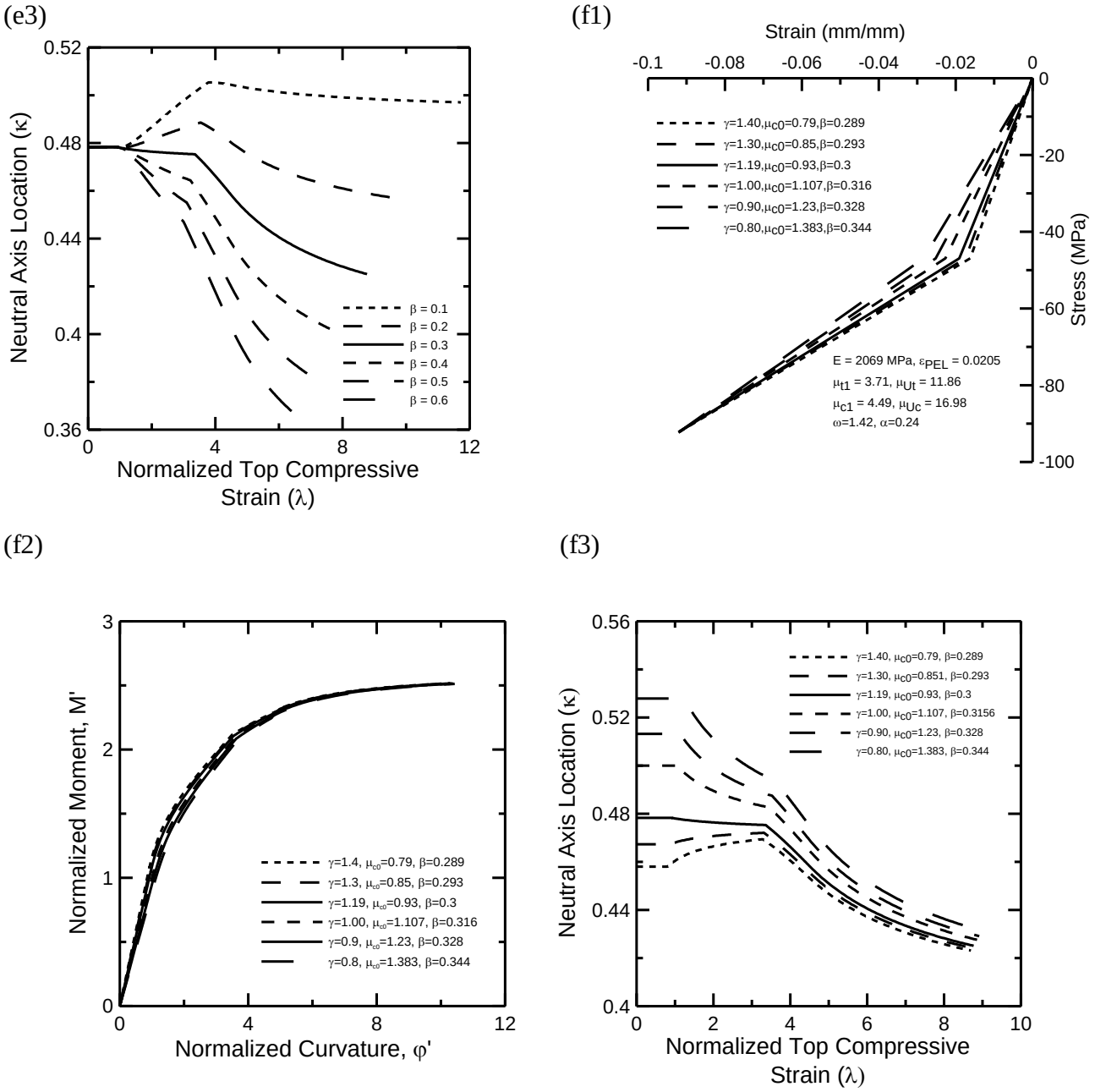

Figure 4: Parametric study of a typical strain softening material

Load Deflection Relationship

When a beam is loaded beyond the modulus of rupture (MOR) in a material with deflection softening behavior, increase the deformation decreases load in the distinct zone (around the loading nose in 3PB) in the cracking region while the rest of the beam undergoes unloading. The length of the localized zone in 3PB with notch or groove was assumed to be 1 mm (around 2% of the beam length). Moment distribution along the

beam is obtained through the static equilibrium of the beam, and the curvature of each point along the beam is obtained though the moment curvature diagram. For epoxy resins, if compressive modulus of elasticity and CYS are greater than the tensile modulus of elasticity and UTS, the shape of the moment curvature diagram greatly depends on the value of the post peak tensile stress. In order to obtain the load deflection response for 3PB from the moment curvature diagram, an array of discrete load steps is defined for a given moment curvature diagram using static equilibrium. The specimen is loaded from 0 to P_{max} in the ascending portion of the moment curvature diagram from 0 to M_{max}. The curvature for this portion is determined directly from the moment curvature diagram. Once the moment reaches MOR, the curvature distribution along the beam in the softening regime depends on the location and the history of the strain at that point. In this study, the length of the localized zone is taken as 1 mm, thus the majority of the sections along the beam will undergo unloading. For the sections with moment less than the moment at limit of proportionality (LOP), the curvature unloads elastically, while for the sections that have been loaded beyond $M_{LOP,}$ the unloading curvature will depend on the recovery percentage of curvature, which can be taken as zero in the monotonic displacement control 3PB test. Knowing the curvature values along the beam for each load step, one can calculate the deflection at the mid-span for each load step using moment area method numerically.

Experimental Results

Tension, compression, and 3PB bending tests were conducted on two hydraulically driven materials test systems (MTS 4411, MTS syntech 1/S), and an electrical desktop load frame (Dual Column Servo-all-Electric Frame Model #:800LE) as shown in Figure 5 at room temperature and at low speed. An interface load cell (interface model SM-1000) was used to measure the axial load in all the tests. Digital image correlation technique (ARAMIS 4M) was used to study the strain fields. This technique recognizes the surface structure of the object to be measured in digital camera images and allocates coordinates to the image pixels. Stress-strain relationship could be found using this technique as it is capable of capturing loads off of the test machine and showing loads in the output file. Dog bone samples with a gage length of 14 mm and a rectangular cross section of 3.18 mm × 3.43 mm were selected to conduct the monotonic tensile tests at the rate of 59 μstr/sec and 493 μstr/sec. Small cubic samples (4 mm × 4 mm × 4 mm) were tested under monotonic compression at the rate of 493 μstr/sec. Small beams with the width of 4 mm, thickness of 10 mm, and length of 60 mm with a groove in the middle of the beam were selected to conduct 3PB tests. Flexural tests were done with different speeds of 0.217 mm/min, 0.542 mm/min, and 1.813 mm/min approximately corresponding to axial strain rates of 59 μstr/sec, 148 μstr/sec, and 493 μstr/sec. Epoxy resin Epon E 863 with a hardener EPI-CURE 3290 using a 100/27 weight ratio was used. Figure 6 illustrates the experimental true stress strain curves from tension and compression tests. Through triggering between load cell and optical system and examining the strain field around the loading nose, Moment curvature response from the 3PB tests were obtained and illustrated in Figure 7. In tension and compression tests, vertical strain along the samples was calculated by taking the average of values of nine stage points located on a sign **“+”**

in the highest strain region. Results of the experiments show a softening behavior beyond the peak point followed by a constant plateau before failure.

(a) (b)

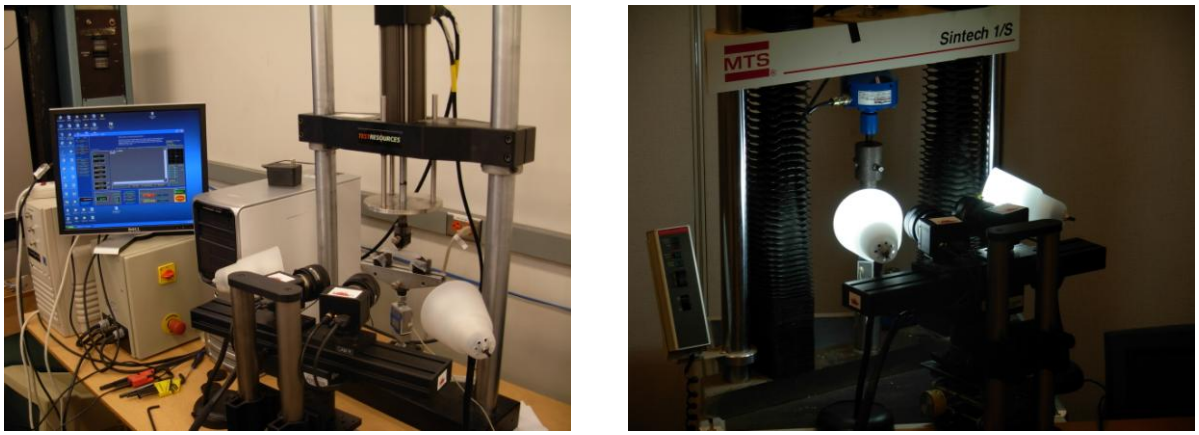

Figure 5. (a) 3PB test set-up; and (b) compression test

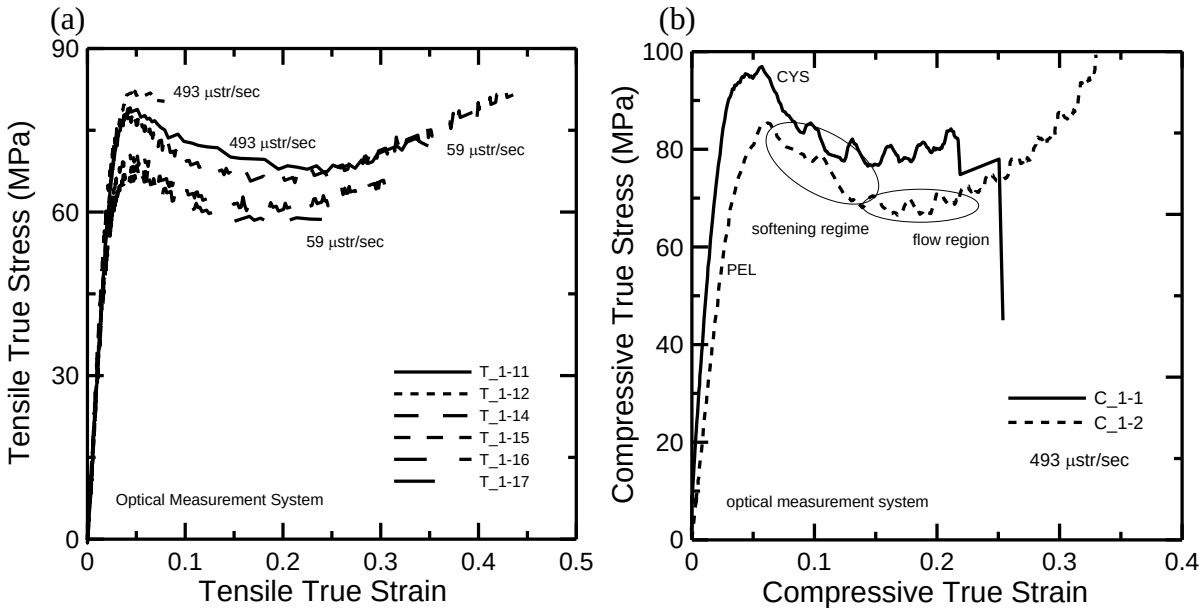

Figure 6. (a) True stress strain tension response; and (b)True stress strain compression behavior

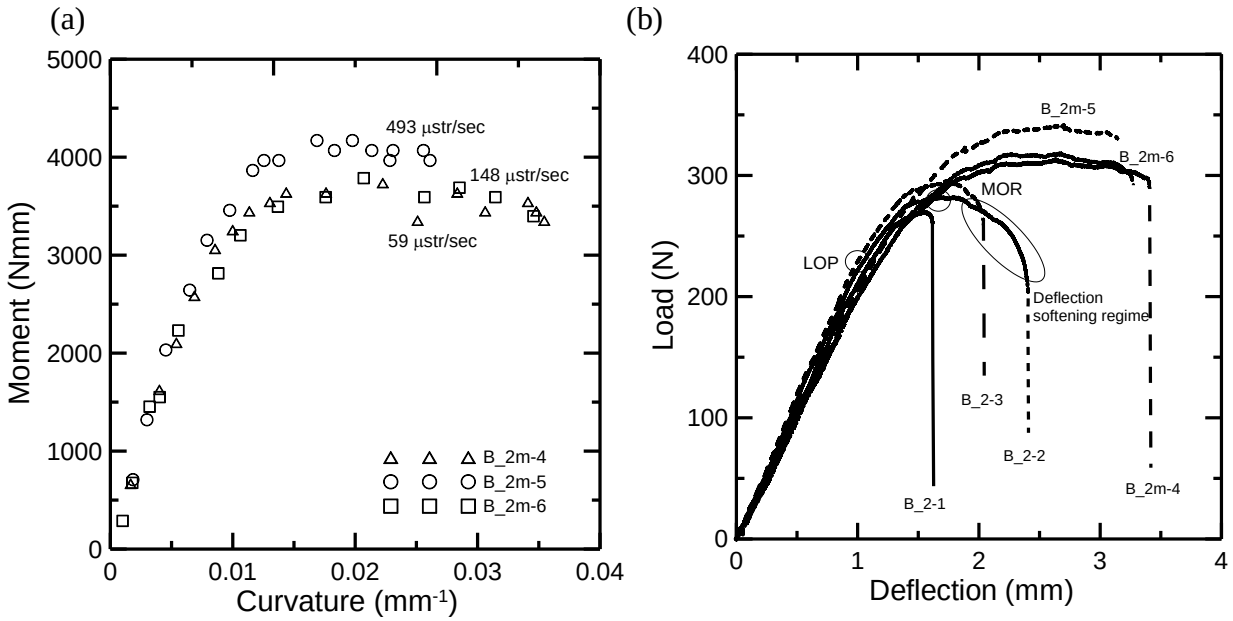

Figure 7. (a) Moment Curvature response for B_2m samples with groove from 3PB test (b) Load deflection response of B_2 and B_2m samples with notch and groove

Flexural Response of Epon E 863

A simulation was used to study the moment curvature and load deflection response of Resin Epon 863 and to evaluate the effects of out of plane loading. The tension and compression stress strain response and the simplified model for strain rate of 493 μstr/sec are shown in Figure 8 (a). Figure 8 (a) also shows the modified model which has been obtained from back calculation of the experimental moment curvature response. The mechanical properties of the simplified model for 493 μstr/sec are presented in Table 12.

Table 12: simplified stress strain mechanical properties of Epon E 863 at 493 μstr/sec

E (MPa)	ε_{PEL} (%)	ε_{Uts} (%)	σ_{Uts} (MPa)	ε_{Ut} (%)	σ_f (MPa)	Ec (MPa)	$\varepsilon_{PEL,c}$ (%)	ε_{CYS} (%)	σ_{CYS} (MPa)	ε_{Uc} (%)
3049	1.62	4.13	79.6	34.9	68	3330	1.86	5.72	96.9	25.4

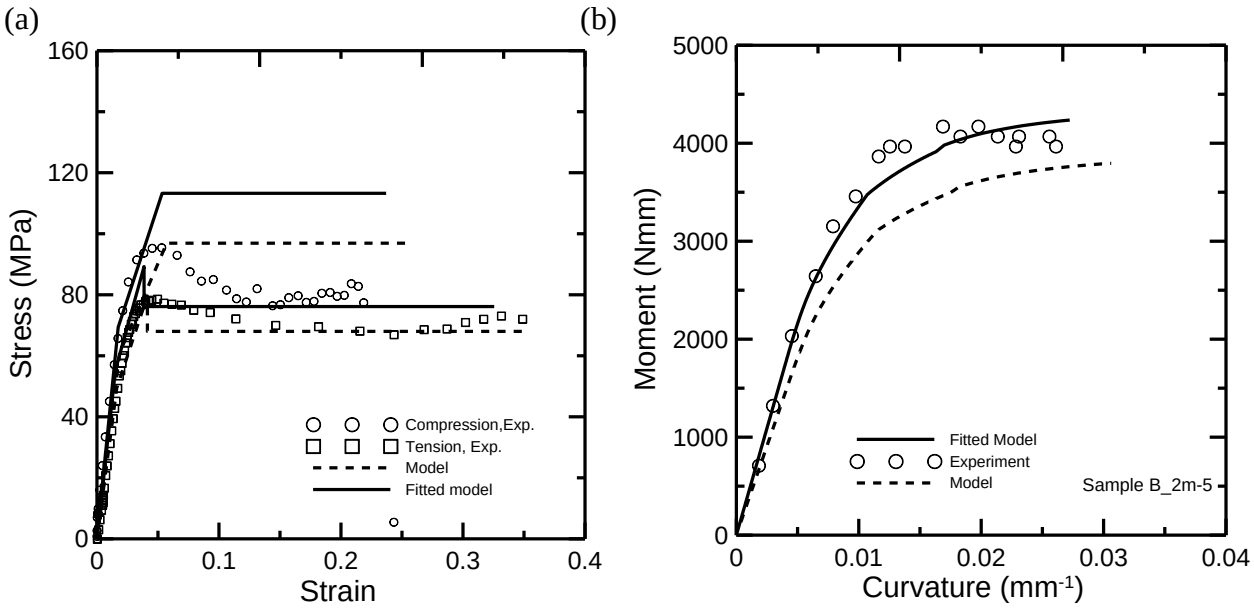

(c)

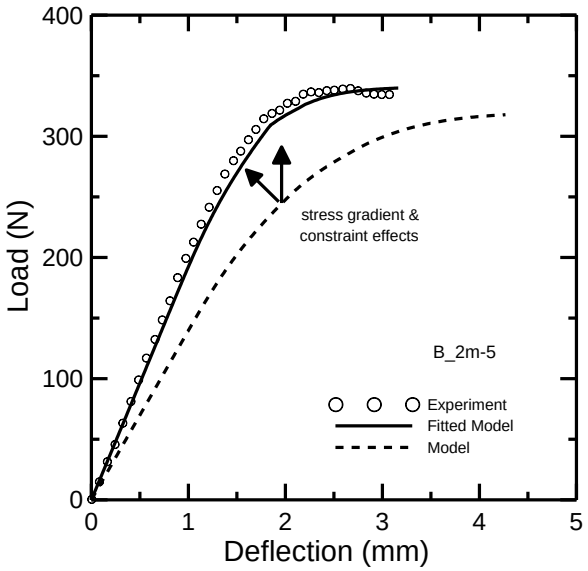

Figure 8: (a) Experiment, model, and fitted model of tension and compression stress strain curve for 493 μstr/sec (b) simulation of moment curvature for sample B_2m-5 with groove and strain rate of 493 μstr/sec; (c) simulation of load deflection for sample B_2m-5 with strain rate of 493 μstr/sec

(a)

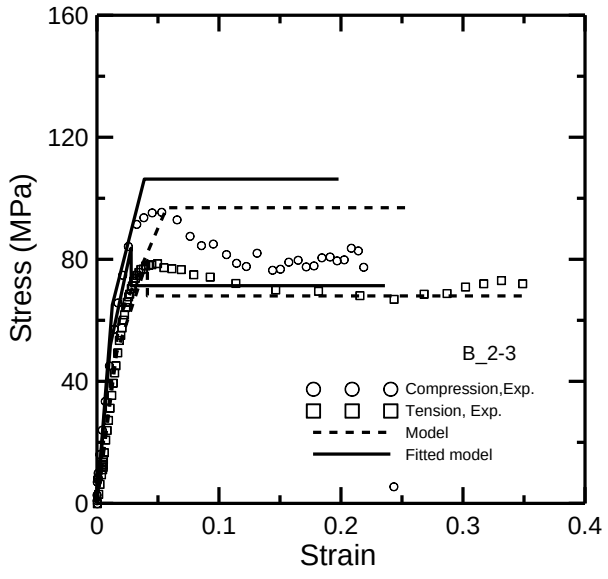

(b)

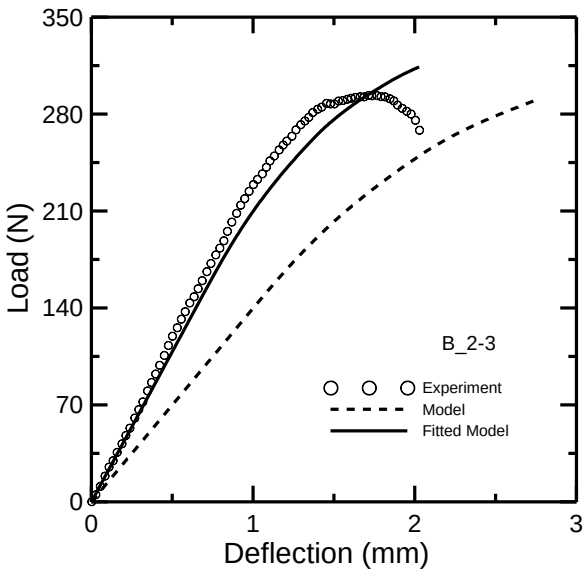

Figure 9: (a) Experiment, model, and fitted model of tension and compression stress strain curve for 493 μstr/sec for B_2-3; and (b) simulation of load deflection for sample B_2-3 with strain rate of 493 μstr/sec

Based on the mechanical properties presented in Table 12, the nine non-dimensional parameters for the model are the following: μ_{c0} = 1.148, μ_{c1} = 3.53, μ_{Uc} = 15.70, μ_{t1} = 2.55, μ_{Ut} = 21.54, γ = 1.09, α = 0.395, β = 0.305, and ω = 1.376. Figure 8 (b) shows the moment curvature curves from the 3PB test (sample B_2m-5 with groove) compared with the simulation results. Figure 8 (b) shows that the tension compression model underpredicts the moment curvature response. Two main reasons for the under prediction are the difference between stress distribution profiles between uniaxial test and bending test, and the effect of lateral constraint in bending tests. In tension and compression tests, the entire volume of the sample is subjected to the same load and has the same probability of failure. However, in a bending test, only a small fraction of the tension and compression regions are subjected to the maximum peak stress. Therefore, the probability of crack nucleation, propagation, and failure development in tension and compression samples is higher than the bending samples. Table 13 compares the limit of proportionality (LOP), modulus of rupture (MOR) of samples B-1, B-2, and B-3 with PEL stress and CYS in compression of sample C-1 (a representative of the compression tests) and PEL stress and UTS in tension of sample T-1 (a representative of the tension tests).

Table 10: PEL, CYS, UTS, LOP, and MOR of samples

Sample	PEL_t (MPa)	UTS (MPa)	PEL_c (MPa)	CYS (MPa)	LOP (MPa)	MOR (MPa)
C-1	-	-	61	97.0	-	-
T-1	49.4	79.6	-	-	-	-
B_2-2	-	-	-	-	81.4	106.08
B_2-3	-	-	-	-	83.3	111.90
B_2m-5	-	-	-	-	83.3	132.2

Results of the uniaxial and bending tests conducted by the authors showed that the ratio of LOP to MOR is up to 14% higher than the ratios of PEL_t to UTS and PEL_c to CYS. In bending tests without axial force, while a part of the cross section is subjected to compression, the other part is subjected to tension. This stress profile results in an increase in tensile and/or compressive modulus of elasticity. To quantify these effects, the authors propose two scaling factors to modify the modulus of elasticity and strength of the material, $E_{mod} = C_1 \times E$, and $\varepsilon_{PEL,mod} = \varepsilon_{PEL} \times C_2/C_1$, and using the same nine non-dimensionalized parameters. Back calculation showed that C_1 for Epon E 863 is around 1.2 to 1.55 while C_2 is between 1.05 and 1.15. Various amounts of imperfections in material directly affect C_2 coefficient but maximum of ($\frac{LOP}{MOR}$ to $\frac{PEL}{UTS}$) and ($\frac{LOP}{MOR}$ to $\frac{PEL}{CYS}$) could be considered as the upper bound. An inverse analysis approach of flexural results will establish a statistical relationship between the compression, tension stress

strain and the flexural response. Inverse analysis showed that C_1 and C_2 for sample B_2m-5 are 1.2 and 1.12 respectively as shown in Figure 8 (b) and (c). Figure 9 illustrate the model and the fitted model as well as experimental and simulated load deflection response for sample B_2-3. The rate of loading in the 3PB test for these sample were 1.813 mm/min (for B_2m-5) and 1.76 mm/min (for B_2-3) corresponding to 493 μstr/sec. C_1 = 1.55 and C_2 = 1.05 were used as the scaling factors for sample B_2-3 as the result of inverse analysis. While the modified models in samples B_2-3 captured the load deflection response up to peak load well, they did not follow the deflection softening behavior up to failure. Results of the parametric study showed that simulation of softening can be improved by changing the post peak tensile level and further adjustments of the other parameters. Modification of tension and compression models in the strain softening region will improve the simulation of the model in the post peak response for bending samples with notch.

Concluding Remarks

Explicit moment curvature equations using nonlinear tension and compression stress strain relation for epoxy resin materials have been developed. A multi-linear stress strain relation for epoxy resin materials, consisting of a constant post peak response in tension and constant yield stress in compression has been used. The material model is described by two intrinsic material parameters: (a) tensile modulus of elasticity and (b) tensile strain at the PEL point, in addition to five non-dimensional parameters for compression and four non-dimensional parameters for tension. A parametric study showed that the normalized moment-curvature response is primarily controlled by the normalized post peak tensile strength, normalized UTS, normalized post compressive PEL stiffness, and normalized CYS. Results show that for materials with small values of post peak tensile strength, reduction of moment curvature response in the softening regime is considerably fast and the response terminates with a relatively low compressive strain. Materials with higher normalized post peak tensile strength have a gradual reduction in the height of the compressive zone, therefore larger deformations are possible. Results show that while very brittle materials have a moment capacity equal to or less than the moment at PEL point, epoxy resin materials with a considerable amount of post peak tensile strength have a moment capacity around 2.5 times the moment at the PEL point. Results showed that for resin materials with post compressive PEL stiffness between 30% and 40% of initial tensile modulus of elasticity with a fixed CYS strain value, the moment capacity is around 2.5 times the moment at the PEL point. Increasing CYS by increasing the post compressive PEL stiffness at high CYS values marginally affects the moment capacity in polymer materials. Simulation of the load deflection response of polymer materials in 3PB test revealed that direct use of tension and compression data under predicts the flexural response. Load deflection response showed that the nominal flexural stress at the peak load estimated by a linear elastic mechanical of material approach is higher than the uniaxial ultimate tensile strength. Curvature distribution along the beam was integrated up to the mid-span of the beam to obtain load deflection response in 3PB. Simulations of the experimental data clearly revealed the effect of stress gradient on the material behavior as the uniaxial tensile and compression tests yields a lower tensile and compression strength than the flexural tests. By applying two scaling factors (C_1 and C_2)

to E and ε_{PEL}, tension and compression stress strain model presented by E, ε_{PEL} and nine normalized parameters (μ_{c0}, μ_{c1}, μ_{Uc} , μ_{t1} , μ_{Ut} , γ, α, β, and ω) could be used for simulations under flexural loading.

Acknowledgments

The authors gratefully acknowledge the support of this research by the Army Research Office, AMSRD-ARL-RO-SI Proposal Number: 49008-EG, Agreement Number: W911NF-07-1-0132, Program Manager: COL. Reed F. Young. We also thank Dr. Dallas Kingsbury from ASU for assistance in compressive, tension, and bending tests.

References

[1] A.S. Wineman, K.R. Rajagopal, K. R. Mechanical Response of Polymers, Cambridge Univeristy Press, New York, (2000).

[2] C. Zhang, I.D. Moore, Nonlinear mechanical response of high density polyethylene. II: Uniaxial constitutive model, Polym. Eng. Sci., 37 (1997), pp. 414-420.

[3] F.Z. Li, J. Pan, Plane stress crack-tip fields for pressure sensitive dilatant materials, J. Appl. Mech., 57 (1990), pp. 40-49.

[4] W. J. Chang, J. Pan, Effects of yield surface shape and round-off vertex on crack-tip fields for pressure sensitive materials, Int. J. Solids Struct., 34 (1997), pp. 3291-3320.

[5] S.Y. Hsu, T.J. Vogler, S. Kyriakides, Inelastic behavior of an AS4/PEEK composite under combined transverse compression and shear, II:modeling, Int. J. Plast., 15 (1999), pp. 807-836.

[6] A. Gilat, R.K. Goldberg, G.D. Roberts, Strain rate sensitivity of epoxy resin in tensile and shear loading, j. of aerosp. eng., ASCE, (2007), pp. 75-89.

[7] J.L. Jordan, J.R. Foley, C.R. Siviour, Mechanical properties of epon 826/DEA epoxy, Mech Time-Depend Mater., 12 (2008), pp. 249-272.

[8] A.D. Mulliken, M.C. Boyce, Mechanics of the rate-dependent elastic-plastic deformation of glassy polymers from low to high strain rates, Int. J. Solids Struct. 43 (2006), pp. 1331–1356.

[9] C.G. Salmon, J.E Johnson, Steel Structures: Design and behavior, 3rd. edition, Harper and Row, New York, (1990)

[10] J.D Littell, C.R. Ruggeri, R.K. Goldberg, G.D. Roberts, W.A. Arnold, W.K. Binienda, Measurement of epoxy resin tension, compression, and shear stress- strain curves over a wide range of strain rates using small test specimens" j. of aerosp. eng., (2008) pp. 162-173.

Appendix

Table 2: Normalized height of tension and compression sub zone for each case

Case	$\frac{h_{c3}}{h}$	$\frac{h_{c2}}{h}$	$\frac{h_{c1}}{h}$	$\frac{h_{t1}}{h}$	$\frac{h_{t2}}{h}$	$\frac{h_{t3}}{h}$
1	-	-	κ	$(1-\kappa)$	-	-
2	-	-	κ	$\frac{\kappa}{\lambda}$	$1-\kappa-\frac{\kappa}{\lambda}$	-
3	-	$\kappa\left(1-\frac{\mu_{c0}}{\lambda}\right)$	$\frac{\mu_{c0}\kappa}{\lambda}$	$(1-\kappa)$	-	-
4	-	-	κ	$\frac{\kappa}{\lambda}$	$\frac{\kappa}{\lambda}(\mu_{t1}-1)$	$1-\kappa-\frac{\mu_{t1}\kappa}{\lambda}$
5	-	$\kappa\left(1-\frac{\mu_{c0}}{\lambda}\right)$	$\frac{\mu_{c0}\kappa}{\lambda}$	$\frac{\kappa}{\lambda}$	$1-\kappa-\frac{\kappa}{\lambda}$	-
6	$\kappa\left(1-\frac{\mu_{c1}}{\lambda}\right)$	$\frac{\kappa}{\lambda}(\mu_{c1}-\mu_{c0})$	$\frac{\mu_{c0}\kappa}{\lambda}$	$(1-\kappa)$	-	-
7	-	$\kappa\left(1-\frac{\mu_{c0}}{\lambda}\right)$	$\frac{\mu_{c0}\kappa}{\lambda}$	$\frac{\kappa}{\lambda}$	$\frac{\kappa}{\lambda}(\mu_{t1}-1)$	$1-\kappa-\frac{\mu_{t1}\kappa}{\lambda}$
8	$\kappa\left(1-\frac{\mu_{c1}}{\lambda}\right)$	$\frac{\kappa}{\lambda}(\mu_{c1}-\mu_{c0})$	$\frac{\mu_{c0}\kappa}{\lambda}$	$\frac{\kappa}{\lambda}$	$1-\kappa-\frac{\kappa}{\lambda}$	-
9	$\kappa\left(1-\frac{\mu_{c1}}{\lambda}\right)$	$\frac{\kappa}{\lambda}(\mu_{c1}-\mu_{c0})$	$\frac{\mu_{c0}\kappa}{\lambda}$	$\frac{\kappa}{\lambda}$	$\frac{\kappa}{\lambda}(\mu_{t1}-1)$	$1-\kappa-\frac{\mu_{t1}\kappa}{\lambda}$

Table 3: Normalized stress at vertices of each tension sub zone for each case

Case	$\frac{\sigma_{t1}}{E\varepsilon_{PEL}}$	$\frac{\sigma_{t2}}{E\varepsilon_{PEL}}$	$\frac{\sigma_{t3}}{E\varepsilon_{PEL}}$
1	$\left(\frac{1-\kappa}{\kappa}\right)\lambda$	-	-
2	1	$1+\alpha\left(\frac{(1-\kappa)\lambda}{\kappa}-1\right)$	-
3	$\left(\frac{1-\kappa}{\kappa}\right)\lambda$	-	-
4	1	$1+\alpha(\mu_{t1}-1)$	ω
5	1	$1+\alpha\left(\frac{(1-\kappa)\lambda}{\kappa}-1\right)$	-
6	$\left(\frac{1-\kappa}{\kappa}\right)\lambda$	-	-

7	1	$1+\alpha(\mu_{t1}-1)$	ω
8	1	$1+\alpha\left(\frac{(1-\kappa)\lambda}{\kappa}-1\right)$	-
9	1	$1+\alpha(\mu_{t1}-1)$	ω

Table 4: Normalized stress at vertices of each compression sub zone for each case

Case	$\frac{\sigma_{c3}}{E\varepsilon_{PEL}}$	$\frac{\sigma_{c2}}{E\varepsilon_{PEL}}$	$\frac{\sigma_{c1}}{E\varepsilon_{PEL}}$
1	-	-	$\gamma\lambda$
2	-	-	$\gamma\lambda$
3	-	$\gamma\mu_{c0}+\beta(\lambda-\mu_{c0})$	$\gamma\mu_{c0}$
4	-	-	$\gamma\lambda$
5	-	$\gamma\mu_{c0}+\beta(\lambda-\mu_{c0})$	$\gamma\mu_{c0}$
6	$\gamma\mu_{c0}+\beta(\mu_{c1}-\mu_{c0})$	$\gamma\mu_{c0}+\beta(\mu_{c1}-\mu_{c0})$	$\gamma\mu_{c0}$
7	-	$\gamma\mu_{c0}+\beta(\lambda-\mu_{c0})$	$\gamma\mu_{c0}$
8	$\gamma\mu_{c0}+\beta(\mu_{c1}-\mu_{c0})$	$\gamma\mu_{c0}+\beta(\mu_{c1}-\mu_{c0})$	$\gamma\mu_{c0}$
9	$\gamma\mu_{c0}+\beta(\mu_{c1}-\mu_{c0})$	$\gamma\mu_{c0}+\beta(\mu_{c1}-\mu_{c0})$	$\gamma\mu_{c0}$

Table 5: Normalized force component of each tension sub-zone for each case

Case	$\frac{F_{t1}}{bhE\varepsilon_{PEL}}$	$\frac{F_{t2}}{bhE\varepsilon_{PEL}}$	$\frac{F_{t3}}{bhE\varepsilon_{PEL}}$
1	$\frac{\lambda\kappa}{2}-\lambda+\frac{\lambda}{2\kappa}$	-	-
2	$\frac{\kappa}{2\lambda}$	$\frac{(\lambda+1)p\kappa}{2\lambda}+\frac{-2\alpha\lambda^2-2\alpha\lambda+2\lambda}{2\lambda}+\frac{\alpha\lambda}{2\kappa},\ p=-2+\alpha\lambda+\alpha$	-
3	$\frac{\lambda\kappa}{2}-\lambda+\frac{\lambda}{2\kappa}$	-	-
4	$\frac{\kappa}{2\lambda}$	$\frac{(2+\alpha\mu_{t1}-\alpha)(\mu_{t1}-1)\kappa}{2\lambda}$	$\frac{-\omega(\lambda+\mu_{t1})\kappa}{\lambda}+\omega$
5	$\frac{\kappa}{2\lambda}$	$\frac{(\lambda+1)p\kappa}{2\lambda}+\frac{-2\alpha\lambda^2-2\alpha\lambda+2\lambda}{2\lambda}+\frac{\alpha\lambda}{2\kappa}$	-
6	$\frac{\lambda\kappa}{2}-\lambda+\frac{\lambda}{2\kappa}$	-	-
7	$\frac{\kappa}{2\lambda}$	$\frac{(2+\alpha\mu_{t1}-\alpha)(\mu_{t1}-1)\kappa}{2\lambda}$	$\frac{-\omega(\lambda+\mu_{t1})\kappa}{\lambda}+\omega$
8	$\frac{\kappa}{2\lambda}$	$\frac{(\lambda+1)p\kappa}{2\lambda}+\frac{-2\alpha\lambda^2-2\alpha\lambda+2\lambda}{2\lambda}+\frac{\alpha\lambda}{2\kappa}$	-
9	$\frac{\kappa}{2\lambda}$	$\frac{(2+\alpha\mu_{t1}-\alpha)(\mu_{t1}-1)\kappa}{2\lambda}$	$\frac{-\omega(\lambda+\mu_{t1})\kappa}{\lambda}+\omega$

Table 6: Normalized force component of each compression sub-zone for each case

Case	$\frac{F_{c3}}{bhE\varepsilon_{PEL}}$	$\frac{F_{c2}}{bhE\varepsilon_{PEL}}$	$\frac{F_{c1}}{bhE\varepsilon_{PEL}}$
1	-	-	$\frac{\gamma\lambda\kappa}{2}$
2	-	-	$\frac{\gamma\lambda\kappa}{2}$
3	-	$\frac{q(\lambda-\mu_{c0})\kappa}{2\lambda}$ $q=2\gamma\mu_{c0}+\beta(\lambda-\mu_{c0})$	$\frac{\gamma\mu_{c0}^2\kappa}{2\lambda}$
4	-	-	$\frac{\gamma\lambda\kappa}{2}$
5	-	$\frac{q(\lambda-\mu_{c0})\kappa}{2\lambda}$	$\frac{\gamma\mu_{c0}^2\kappa}{2\lambda}$
6	$\frac{s(\lambda-\mu_{c1})\kappa}{\lambda}$ $s=\gamma\mu_{c0}+\beta(\mu_{c1}-\mu_{c0})$	$\frac{r(\mu_{c1}-\mu_{c0})\kappa}{2\lambda}$ $r=2\gamma\mu_{c0}+\beta(\mu_{c1}-\mu_{c0})$	$\frac{\gamma\mu_{c0}^2\kappa}{2\lambda}$
7	-	$\frac{q(\lambda-\mu_{c0})\kappa}{2\lambda}$	$\frac{\gamma\mu_{c0}^2\kappa}{2\lambda}$
8	$\frac{s(\lambda-\mu_{c1})\kappa}{\lambda}$	$\frac{r(\mu_{c1}-\mu_{c0})\kappa}{2\lambda}$	$\frac{\gamma\mu_{c0}^2\kappa}{2\lambda}$
9	$\frac{s(\lambda-\mu_{c1})\kappa}{\lambda}$	$\frac{r(\mu_{c1}-\mu_{c0})\kappa}{2\lambda}$	$\frac{\gamma\mu_{c0}^2\kappa}{2\lambda}$

Table 7. Normalized moment arm to neutral axis of each tension sub-zone in each case

Case	$\frac{Z_{t1}}{h}$	$\frac{Z_{t2}}{h}$	$\frac{Z_{t3}}{h}$
1	$\frac{2}{3}(1-\kappa)$	-	-
2	$\frac{2\kappa}{3\lambda}$	$\frac{y_1\kappa^2+y_2\kappa-2\alpha\lambda^2}{3\lambda(p\kappa-\alpha\lambda)}, y_1=3\lambda-3-\alpha\lambda+\alpha-2\alpha\lambda^2, y_2=4\alpha\lambda^2+\lambda(\alpha-3)$	-
3	$\frac{2}{3}(1-\kappa)$	-	-
4	$\frac{2\kappa}{3\lambda}$	$\frac{y_4\kappa}{3y_5\lambda}, y_4=3\mu_{t1}+3+2\alpha\mu_{t1}^2-\alpha\mu_{t1}-\alpha,\ y_5=2+\alpha(\mu_{t1}-1)$	$\frac{1}{2}\left(1-\frac{(\lambda-\mu_{t1})\kappa}{\lambda}\right)$
5	$\frac{2\kappa}{3\lambda}$	$\frac{y_1\kappa^2+y_2\kappa-2\alpha\lambda^2}{3\lambda(p\kappa-\alpha\lambda)}$	-
6	$\frac{2}{3}(1-\kappa)$	-	-
7	$\frac{2\kappa}{3\lambda}$	$\frac{y_4\kappa}{3y_5\lambda}$	$\frac{1}{2}\left(1-\frac{(\lambda-\mu_{t1})\kappa}{\lambda}\right)$
8	$\frac{2\kappa}{3\lambda}$	$\frac{y_1\kappa^2+y_2\kappa-2\alpha\lambda^2}{3\lambda(p\kappa-\alpha\lambda)}$	-
9	$\frac{2\kappa}{3\lambda}$	$\frac{y_4\kappa}{3y_5\lambda}$	$\frac{1}{2}\left(1-\frac{(\lambda-\mu_{t1})\kappa}{\lambda}\right)$

Table 8. Normalized moment arm to neutral axis of each compression sub-zone in each case

Case	$\frac{Z_{c3}}{h}$	$\frac{Z_{c2}}{h}$	$\frac{Z_{c1}}{h}$
1	-	-	$\frac{2\kappa}{3}$
2	-	-	$\frac{2\kappa}{3}$
3	-	$\frac{y_3\kappa}{3q\lambda},\ y_3 = 3\gamma\mu_{c0}^2 - \mu_{c0}\beta\lambda - \beta\mu_{c0}^2 + 3\gamma\mu_{c0}\lambda + 2\beta\lambda^2$	$\frac{2\mu_{c0}\kappa}{3\lambda}$
4	-	-	$\frac{2\kappa}{3}$
5	-	$\frac{y_3\kappa}{3q\lambda}$	$\frac{2\mu_{c0}\kappa}{3\lambda}$
6	$\frac{(\lambda+\mu_{c1})\kappa}{2\lambda}$	$\frac{y_6\kappa}{3r\lambda}, y_6 = 3\gamma\mu_{c0}^2 - \mu_{c0}\beta\mu_{c1} - \beta\mu_{c0}^2 + 3\gamma\mu_{c0}\mu_{c1} + 2\beta\mu_{c1}^2$	$\frac{2\mu_{c0}\kappa}{3\lambda}$
7	-	$\frac{y_3\kappa}{3q\lambda}$	$\frac{2\mu_{c0}\kappa}{3\lambda}$
8	$\frac{(\lambda+\mu_{c1})\kappa}{2\lambda}$	$\frac{y_6\kappa}{3r\lambda}$	$\frac{2\mu_{c0}\kappa}{3\lambda}$
9	$\frac{(\lambda+\mu_{c1})\kappa}{2\lambda}$	$\frac{y_6\kappa}{3r\lambda}$	$\frac{2\mu_{c0}\kappa}{3\lambda}$

Table 9: Auxiliary transition points in the stress strain development diagram

A(γ)	$\frac{\sqrt{\gamma}-1}{\gamma-\sqrt{\gamma}}$
B(γ,β,μ_{c0})	$\frac{\mu_{c0}(\beta-\gamma)+\sqrt{\mu_{c0}^2\gamma(\gamma-\beta)+\beta}}{\beta}$
C(γ,α,μ_{t1})	$\sqrt{\frac{\alpha(\mu_{t1}-1)^2+2\mu_{t1}-1}{\gamma}}$
D(γ,β,μ_{c0},μ_{c1})	$\frac{1+\gamma\mu_{c0}^2+\beta(\mu_{c1}^2-\mu_{c0}^2)}{2(\gamma\mu_{c0}+\beta(\mu_{c1}-\mu_{c0}))}$
E(γ,β,μ_{c0},α,μ_{t1})	$\frac{\mu_{c0}(\beta-\gamma)+\sqrt{\gamma\mu_{c0}^2(\gamma-\beta)+\alpha\beta\mu_{t1}^2+\beta(1-\alpha)(2\mu_{t1}-1)}}{\beta}$
F(γ,α,μ_{t1},μ_{Ut},ω)	$\sqrt{\frac{2\omega(\mu_{Ut}-\mu_{t1})+\alpha(\mu_{t1}-1)^2+2\mu_{t1}-1}{\gamma}}$
G(γ,β,μ_{c0},μ_{c1},α,μ_{t1})	$\frac{\alpha\mu_{t1}^2+(\alpha-1)(1-2\mu_{t1})+\gamma\mu_{c0}^2+\beta(\mu_{c1}^2-\mu_{c0}^2)}{2(\gamma\mu_{c0}+\beta(\mu_{c1}-\mu_{c0}))}$
H(γ,β,μ_{c0},α,μ_{t1},μ_{Ut},ω)	$\frac{\mu_{c0}(\beta-\gamma)+\sqrt{2\omega\beta(\mu_{Ut}-\mu_{t1})+\gamma\mu_{c0}^2(\gamma-\beta)+\alpha\beta\mu_{t1}^2+\beta(1-\alpha)(2\mu_{t1}-1)}}{\beta}$
I(γ,β,μ_{c0},μ_{c1},α,μ_{t1},μ_{Ut},ω)	$\frac{2\omega(\mu_{Ut}-\mu_{t1})+\alpha\mu_{t1}^2+(\alpha-1)(1-2\mu_{t1})+\gamma\mu_{c0}^2+\beta(\mu_{c1}^2-\mu_{c0}^2)}{2(\gamma\mu_{c0}+\beta(\mu_{c1}-\mu_{c0}))}$

Table 10: Neutral axis depth ratio, and moment for each case

Case	κ_i	M'_i
1	$\frac{-1+\sqrt{\gamma}}{\gamma-1}$	$2\lambda(\gamma-1)\kappa_1^2+6\lambda\kappa_1-6\lambda+\frac{2\lambda}{\kappa_1}$
2	$\frac{-\lambda\left(\alpha(\lambda+1)-1-\sqrt{-\alpha+1+\alpha\gamma\lambda^2}\right)}{-t_1+\gamma\lambda^2}$, $t_1=\alpha(\lambda+1)^2-2\lambda-1$	$\frac{\left((1-\alpha)(3\lambda^2-1)-2\lambda^3(\alpha-\gamma)\right)\kappa_2^2}{\lambda^2}+t_9\kappa_2+t_{10}+\frac{2\alpha\lambda}{\kappa_2}$ $t_9=6(\alpha(\lambda+1)-1)$, $t_{10}=3(1-\alpha(1+2\lambda))$
3	$\frac{\lambda\left(\lambda-\sqrt{t_2}\right)}{\lambda^2-t_2}$, $t_2=$ $(\lambda-\mu_{c0})^2(\beta-\gamma)+\gamma\lambda^2$	$\frac{\left(t_5-2\lambda^3(1-\beta)\right)\kappa_3^2}{\lambda^2}+6\lambda(\kappa_3-1)+\frac{2\lambda}{\kappa_3}$, $t_5=(\beta-\gamma)\mu_{c0}\left(\mu_{c0}^2-3\lambda^2\right)$
4	$\frac{2\omega\lambda}{t_4+\gamma\lambda^2}$, $t_4=$ $1+2\omega\lambda+2\mu_{t1}(\omega-1)-\alpha(\mu_{t1}-1)^2$	$\frac{\left(t_7+t_8+2\left(\gamma\lambda^3+\alpha\mu_{t1}^3\right)\right)\kappa_4^2}{\lambda^2}-6\omega\kappa_4+3\omega$ $t_7=(1-\alpha)(3\mu_{t1}^2-1)$, $t_8=3\omega(\lambda^2-\mu_{t1}^2)$
5	$\frac{\lambda\left(\alpha(\lambda+1)-1-\sqrt{-\alpha+1+\alpha t_2}\right)}{t_1-t_2}$	$\frac{\left(t_5-2\lambda^3(\alpha-\beta)+(1-\alpha)(3\lambda^2-1)\right)\kappa_5^2}{\lambda^2}+t_9\kappa_5+t_{10}+\frac{2\alpha\lambda}{\kappa_5}$
6	$\frac{\lambda\left(\lambda-\sqrt{t_3}\right)}{\lambda^2-t_3}$, $t_3=t_2-\beta(\lambda-\mu_{c1})^2$	$\frac{\left(t_5-t_6-2\lambda^3\right)\kappa_6^2}{\lambda^2}+6\lambda(\kappa_6-1)+\frac{2\lambda}{\kappa_6}$, $t_6=\beta\mu_{c1}\left(\mu_{c1}^2-3\lambda^2\right)$
7	$\frac{2\omega\lambda}{t_4+t_2}$	$\frac{\left(t_5+t_7+t_8+2\left(\beta\lambda^3+\alpha\mu_{t1}^3\right)\right)\kappa_7^2}{\lambda^2}-6\omega\kappa_7+3\omega$
8	$\frac{\lambda\left(\alpha(\lambda+1)-1-\sqrt{-\alpha+1+\alpha t_3}\right)}{t_1-t_3}$	$\frac{\left(t_5-t_6+3\lambda^2(1-\alpha)+\alpha\left(1-2\lambda^3\right)-1\right)\kappa_8^2}{\lambda^2}$ $+t_9\kappa_8+t_{10}+\frac{2\alpha\lambda}{\kappa_8}$
9	$\frac{2\omega\lambda}{t_4+t_3}$	$\frac{\left(t_5-t_6-3\mu_{t1}^2(\omega+\alpha-1)+\alpha\left(1+2\mu_{t1}^3\right)+3\omega\lambda^2\right)\kappa_9^2}{\lambda^2}$ $-6\omega\kappa_9+3\omega$